

Investigating the Relative Contributions of Charge Deposition and Turbulence in Organizing Charge within a Thunderstorm

MATTHEW D. BROTHERS AND ERIC C. BRUNING

Texas Tech University, Lubbock, Texas

EDWARD R. MANSELL

NOAA/OAR/National Severe Storms Laboratory, Norman, Oklahoma

(Manuscript received 5 January 2018, in final form 9 July 2018)


ABSTRACT

Large-eddy-resolving simulations using the Collaborative Model for Multiscale Atmospheric Simulation (COMMAS), which contains microphysical charging and branched-lightning parameterizations, produce much more complex net charge structures than conventionally visualized from previous observations, simulations, and conceptual diagrams. Many processes contribute to the hydrometeor charge budget within a thunderstorm, including advection, hydrometeor differential sedimentation, subgrid turbulent mixing and diffusion, ion drift, microphysical separation, and the attachment of ion charge deposited by the lightning channel. The lightning deposition, sedimentation, and noninductive charging tendencies contribute the most overall charge at relatively large scales, while the advection tendency, from resolved turbulence, provides the most “texture” at small scales to the net charge density near the updraft region of the storm. The scale separation increases for stronger storm simulations. In aggregate, lightning deposition and sedimentation resemble the smoother distribution of the electric potential, while evidence suggests individual flashes could be responding to the fine texture in the net charge. The clear scale separation between the advection and other net charge tendencies suggest the charge advection is most capable of providing net charge texture; however, a clear-cut causality is not obtained from this study.

1. Introduction

Thunderstorm electrification studies have revealed numerous aspects of lightning and charge characteristics, yet the spatial and temporal details of the charge distribution are still being uncovered. The existence of a mixed-phase updraft within a thunderstorm results in ice–ice collisions where the hydrometeors gain charge in the presence of liquid water as a part of the noninductive charging mechanism (Reynolds et al. 1957; Saunders 2008). The charge sign that riming graupel gains from these ice–ice collisions depends on the temperature, rime accretion rate, and liquid water content within the cloud (Takahashi 1978; Saunders and Peck 1998). As a result of these hydrometeors being advected away from

charging regions and hydrometeor sedimentation due to differential vertical velocities, typical storms contain an upper positive charge region consisting of ice crystals, a main negative charge region consisting of both graupel and ice crystals, and a lower positive charge region consisting of graupel. This simplistic representation of how charge is organized within a thunderstorm is known as the tripole model (Williams et al. 1989; MacGorman et al. 2001). Studies that analyzed electric field soundings through convective regions of various storm modes concluded that four charge regions may exist near the updraft region of the storm, while up to six charge regions may exist outside the updraft region of the storm (Stolzenburg et al. 1998). Supercell simulations from Calhoun et al. (2014) revealed a complex evolution of charge structure with six to seven different layers frequently present with a relatively larger horizontal extent. Multiple studies have looked into the possible mechanisms for how these charge structures become more complex than the tripole model.

 Denotes content that is immediately available upon publication as open access.

Corresponding author: Matthew D. Brothers, mbrothers18@gmail.com

DOI: 10.1175/JAS-D-18-0007.1

© 2018 American Meteorological Society. For information regarding reuse of this content and general copyright information, consult the AMS Copyright Policy (www.ametsoc.org/PUBSReuseLicenses).

Charge deposited by the lightning channel may complicate the charge structure within a thunderstorm (Coleman et al. 2003). The net result of the discharge is to neutralize or reduce electric energy built up within the storm and decrease the electric field magnitude between regions of charge. Coleman et al. (2003) reported that vertical profiles of thunderstorm electric fields through multicellular storms in New Mexico found abrupt change of sign in the electric field after numerous flashes traversed near the instrument's location. This change was attributed to charge displacement by the lightning channel. Additionally, two specific lightning channels observed by New Mexico Tech's Lightning Mapping Array (LMA) avoided regions where a preceding flash traveled through, which implied that the charge density and potential of those regions had been reduced by charge being deposited from the preceding flash. Coleman et al. (2003) concluded that the storm charge structure became more complex with the net effect of charge deposited by the lightning channel. However, the overall effect on the net charge structure from lightning in comparison to other methods for organizing charge within a thunderstorm is unclear.

Bruning and MacGorman's (2013) analysis of flash extent density and mean flash area grids from a high-precipitation supercell using the Oklahoma LMA revealed few flashes in the downshear anvil, which were all relatively large. On the southern flank of the same storm where the development of a new lightning hole had occurred, the smallest flash areas were found along with the greatest number of flash initiations. These results led Bruning and MacGorman (2013) to claim that an inverse relationship between lightning initiation and flash size existed, verifying their electrostatic prediction. Thus, it was suggested that because of the complex flow in and around the updraft, regions of charged hydrometeors could be broken into smaller pockets in addition to the possible presence of small charge separation regions. Therefore, since the lightning flash will reflect the geometry of these charge regions (MacGorman et al. 2001), the channel growth may be contained to these smaller pockets of charge with proportionally larger charge densities where breakdown can be achieved. Simulations conducted by Calhoun et al. (2014) also revealed details of the dependence of lightning on storm kinematics.

The net charge budget tendency equation for charge ρ_n on a given hydrometeor type can be used to investigate how these smaller pockets of charge develop. The equation, following Mansell et al. (2005), is

$$\frac{\partial \rho_n}{\partial t} = -\nabla \cdot (\rho_n \mathbf{V}) + \nabla \cdot (K_h \nabla \rho_n) + \frac{\partial (V_{tn} \rho_n)}{\partial z} + S_n, \quad (1)$$

where the right-hand-side terms in order represent the charge transport by advection (including resolved turbulent eddies), subgrid turbulent mixing, sedimentation, and sum of local source and sink terms (i.e., charge separation, ion attachment, and change of hydrometeor category). These contributors represent all the ways charge can be separated and redistributed throughout a thunderstorm. The goal of the authors in this present study was to design an experiment whereby quantifying the components of (1) results in a better understanding of the processes that result in the spatial distribution and polarity of charged hydrometeors.

Inferred positive and negative charge (potential) regions within a storm can be determined with LMA source points (Rison et al. 1999; Shao and Krehbiel 1996; Mazur 2002); however, these regions can only be identified where a lightning channel propagated through a storm, and no magnitude of charge can be assigned. These LMA source points could also be useful for identifying regions within the storm impacted by lightning charge deposition, yet no relative comparison to other contributors can be made from LMA source points alone. To study the complexity seen in a thunderstorm's charge distribution and influence of each charge contributor in (1) throughout the entire thunderstorm, a storm-scale modeling approach was explored.

2. Methods

a. Simulation model

This work employed the Collaborative Model for Multiscale Atmospheric Simulation (COMMAS; Wicker and Wilhelmson 1995; Mansell et al. 2010), which is based on the equation set of Klemp and Wilhelmson (1978). The microphysics are modeled by the NSSL two-moment, four-ice-category bulk scheme (Mansell et al. 2010; Ziegler 1985; Mansell and Ziegler 2013), which predicts the mass mixing ratio and number concentration for cloud droplets, rain, cloud ice, snow, graupel, and hail. The bulk particle densities of graupel and hail are also predicted, along with the number concentration of cloud condensation nuclei (CCN). Here, the CCN number mixing ratio q_{ccn} was set to a uniform value of $(1 \times 10^9)/\rho_{air0}$ (kg^{-1}), where $\rho_{air0} = 1.225 \text{ kg m}^{-3}$. The CCN number concentration thus decreases exponentially with height as $1 \times 10^9 (\rho_{air}/\rho_{air0})$. Noninductive charge separation was parameterized following Saunders and Peck (1998), as modified in Mansell et al. (2010) and Fierro and Mansell (2017) and inductive charging and small ion processes as in Mansell et al. (2005). Lightning discharges were simulated by the three-dimensional stochastic branched-lightning scheme of Mansell (2002).

The simulations were run until the storms' evolution matched the basic mode of the observations and electrical properties had matured. For each case, the storm was simulated using two different horizontal grid spacings of 125 and 1000 m while the vertical resolution remained constant (not stretched) at 125 m up to a model-top height of 20 km. The horizontal and vertical simulated lightning grid spacing remained at 125 m for all simulations. A model time step of 1 s was used for each of the simulations. The simulations were initiated with a warm bubble with varying size, depth, and temperature perturbation shown in Table 1.

The storms were simulated at two resolutions to help isolate the influence of turbulence on the storm charge structure. Bryan et al. (2003) made the argument that most thunderstorm models run into the issue of inadequate resolution for the desired phenomena. A length-scale ratio (between atmospheric phenomena and grid spacing) of about 100 works well for planetary boundary layer studies to resolve turbulent flow. To achieve the same length-scale ratio when simulating deep moist convection, a grid spacing on the order of 100 m is needed. Therefore, simulations using 1000-m horizontal grid spacing would not be capable of resolving large-eddy motions (unlike simulations with 125-m horizontal grid spacing), thus impacting the simulated thunderstorm's flow structure, the advection of charge-carrying hydrometeors, and the complexity of the simulated thunderstorm's charge structure.

b. Environmental soundings

Simulations for this study made use of one observed (Fig. 1) and one idealized (Fig. 2) sounding. The classic Weisman–Klemp sounding (Weisman and Klemp 1982) was used along with an atmospheric sounding from the Kinematic Texture and Lightning (KTaL) field campaign at Texas Tech University over summers 2014–16. The simulations in this study included the Weisman–Klemp (WK) supercell and a multicellular case (KTaL071015B). The Weisman–Klemp sounding was used to simulate a generic supercell thunderstorm and the lightning distribution associated with that storm mode. The specific sounding used in this study had a surface potential temperature of 300 K and surface mixing ratio of 15 g kg^{-1} . The depth of the shear layer was 5 km with a hodograph length of 40 m s^{-1} through the depth of the shear layer. The atmospheric soundings from KTaL were used to simulate storms in an environment similar to those observed by the west Texas LMA and scanned by the Texas Tech Ka-band Doppler radars (Gunter and Schroeder 2015; Chmielewski and Bruning 2016). The KTaL071015B sounding had a surface potential temperature of 311 K and surface mixing

TABLE 1. Summary of simulation-specific details for the two storm cases being analyzed in this study. Note that $1 \text{ kt} = 0.51 \text{ m s}^{-1}$.

Initialization specifics	KTaL071015B	WK supercell
Domain (km)	40×40	60×60
Simulation duration (s)	5400	4200
Storm mode	Multicell	Supercell
Temperature perturbation (K)	1	2
Horizontal bubble radius (m)	8000	10 000
Vertical bubble radius (m)	1400	1400
Additional forcing region	Yes	No
Mixed-layer CAPE (J kg^{-1})	1881	3132
0–6-km shear (kt)	15	70

ratio of 14.3 g kg^{-1} . As seen in Table 1, the vertical wind shear present in the KTaL071015B sounding was much less than that from the WK supercell sounding.

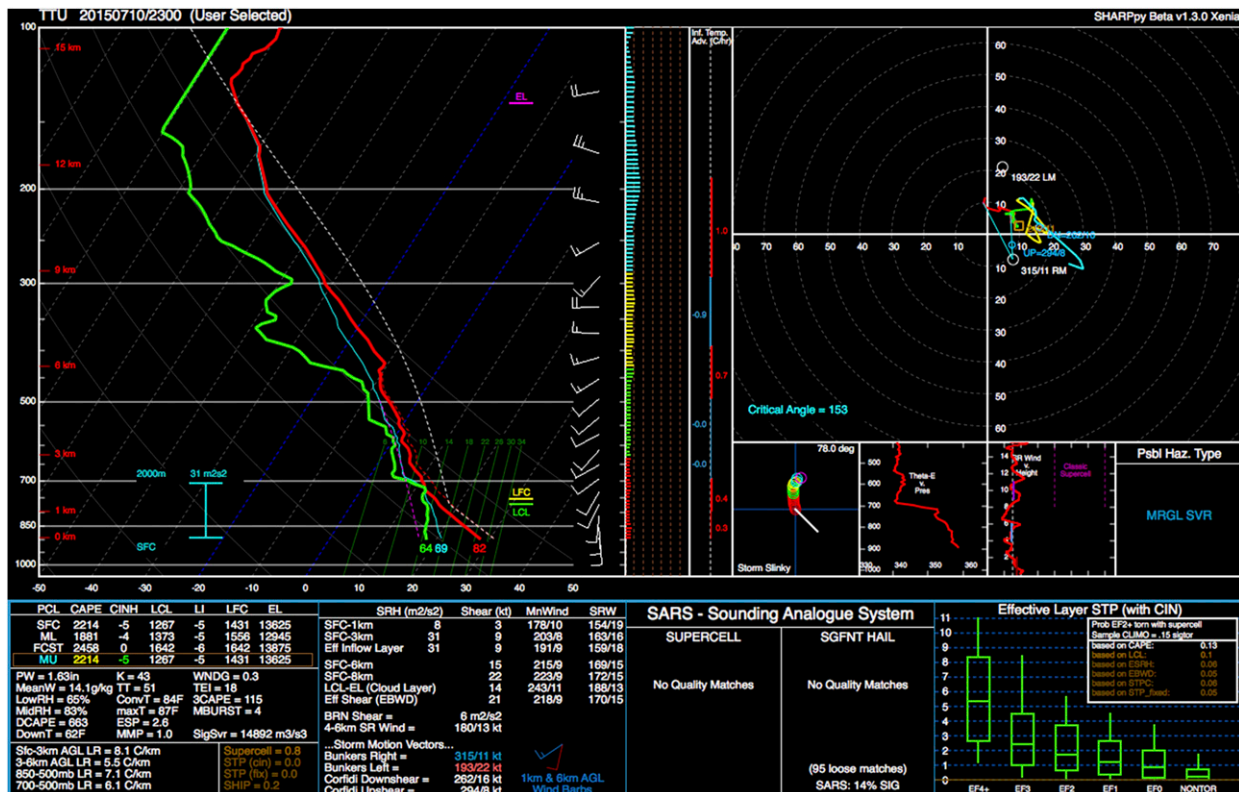
c. Analysis of charge budget contributors

Model output from COMMAS was expanded to include processes contributing to net charge. The advection (ADV), lightning deposition (LGT), sedimentation (SED), subgrid mixing (MIX), ion drift (ION), and non-inductive charging (NIC) processes from the charge tendency equation [(1)] were analyzed independently in this work. The charge contribution fields within COMMAS were accumulated and saved to model output files at 30-s intervals. These contributors were analyzed near the peak in the storms' electrical activity, a time with relatively high flash rates and small flash areas.

1) TEXTURE

Some charge contributors produced a large amount of the same sign of charge in a few contiguous regions (i.e., sedimentation and lightning deposition), while others (i.e., charge advection) transported equal amounts of charge but with many changes in sign in adjoining regions. These smaller pockets of charge within the net charge density are a form of spatial inhomogeneity. Therefore, in order to characterize the relative contribution from each process, the magnitude of accumulated charge as well as this inhomogeneity was analyzed. The inhomogeneity may also have some scale dependence, and to encompass all of these ideas, we use “texture” as a shorthand throughout this study, with the sense that more textured regions have more small-scale spatial inhomogeneity.

Texture has been a term used in the literature by remote sensing geographers to describe a scale-specific variation that provides structural information to the interpreter (Hay et al. 1996). Some approaches have used the gray-level variance of a remote sensing image as a texture parameter along with other methods such as homogeneity, dissimilarity, correlation, contrast, entropy, and energy for mapping land-use regions (Herold et al. 2003;



To quantify the texture of the simulated thunderstorm's charge density, a $5 \times 5 \times 5$ pixel moving window was used to collect values of net charge tendency and calculate the standard deviation of those values. That standard deviation value was then assigned to the grid point at the center of the window. However, the shortcoming of this method was that large values of net charge tendency dominated over the variation in sign of net charge tendency. Therefore, this aspect of texture was lost in the analysis and ultimately led to the use of Fourier analysis to describe the texture of these charge-contributing fields where the magnitude of a signal was just as important as the variation of sign.

For each simulation, the average spectrum from neighboring grid cells was calculated near the updraft region of the storm as well as outside the updraft region. The average spectrum was calculated by finding the mean amplitude at each wavenumber from all the profiles in a 5×5 box, normal to the direction of the profile, centered on a manually selected grid cell. This specific neighborhood averaging method was chosen because it successfully smooths out the spectrum while preserving the location and spread of the largest spectral peaks. Also calculated was the cumulative variance from longest to shortest resolved wavelength to show the total variance that had been accumulated at given wavenumbers. Since the sum of the discrete spectral components up to the Nyquist frequency from the FFT equals

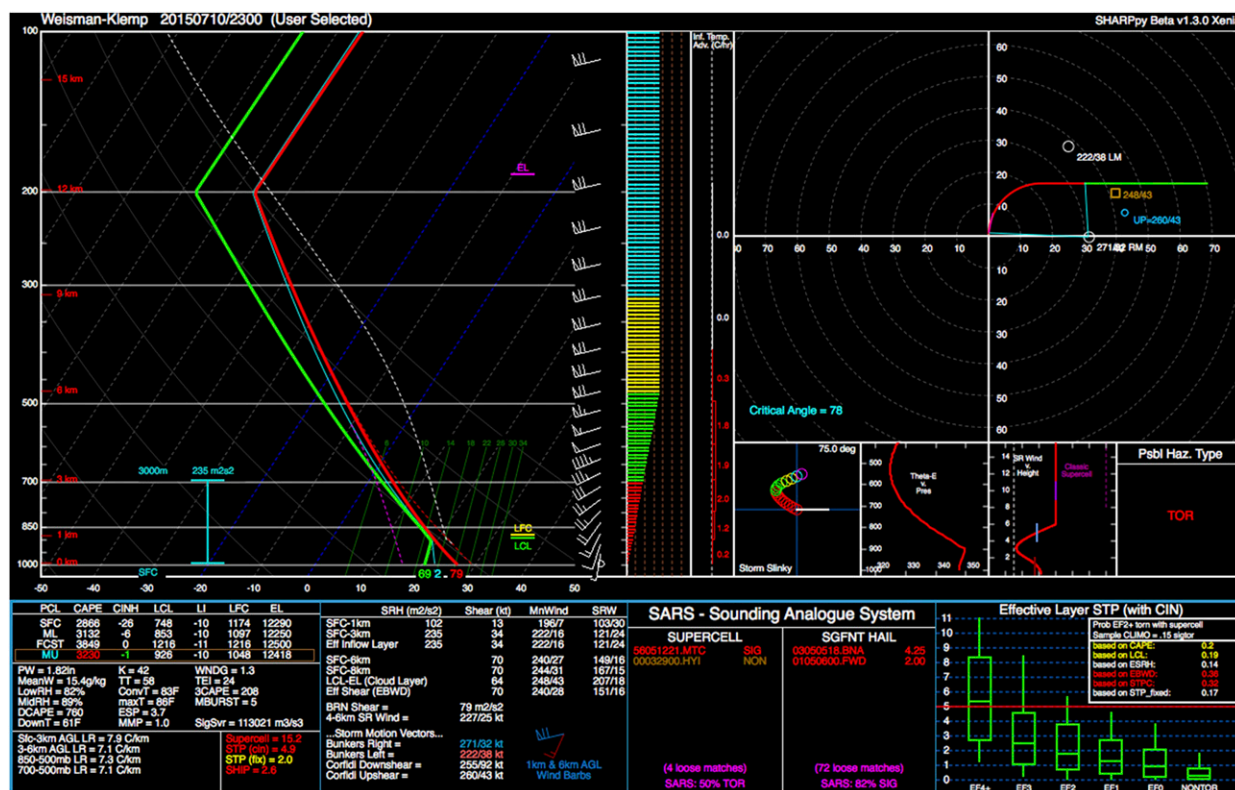


FIG. 2. As in Fig. 1, but for the supercellular environment (WK supercell case).

the variance of the signal, this percentage was calculated by dividing the accumulated variance up to a given wavenumber by the total variance of the signal. This was used to determine whether certain charge contributors were varying more at smaller scales (large wavenumber) or at larger scales (small wavenumber).

The “near updraft” regions were manually selected in regions of the storm with high flash rates in close proximity (at or within a few grid points) to vertical velocities exceeding 20 m s^{-1} . The “outside updraft” region was manually selected downshear from the updraft generally in a region with lower flash rates and primarily horizontal flow. This allowed for the comparison of these textured charge tendencies not only between storm simulations but also in various regions within each storm. By comparing all the charge budget contributors within the storm, the scale-resolved contribution from charge deposited by a lightning channel can be obtained relative to the other processes that separate and redistribute charge.

3. Results

This paper examined the differences between the KTaL071015B and WK supercell cases as these two

simulations have different simulated convective modes and electrical activity. Figure 3 displays the flash extent density (FED; count per grid box) and mean flash area (km^2) over the previous 30 s of the KTaL071015B case near the simulation’s peak in electrical activity with a flash rate of 22 min^{-1} and mean flash area of 30 km^2 . As expected, the inverse relationship between these two quantities held true for this simulation. Regions of high FED (≥ 5) resulted in mean flash areas around 40 km^2 , while areas of low FED (≤ 2) resulted in mean flash areas around 80 km^2 . Figure 3 also shows the flash extent density (count per grid) and mean flash area (km^2) over the previous 30 s of the WK supercell case near the simulation’s peak in electrical activity with a flash rate of 175 min^{-1} and mean flash area of 105 km^2 . Once again, a general inverse relationship between the spatial distributions of these two quantities was found for this simulation. However, with a larger and higher-flash-rate storm, a greater range of mean flash areas were seen throughout various regions of the simulation. Regions of high FED (≥ 30) resulted in mean flash areas around 100 km^2 , while areas of low FED (≤ 2) resulted in mean flash areas of 210 km^2 or greater.

Figure 4 shows the vertical cross-sectional view (along the black lines in Fig. 3) of net charge density and electric potential for the multicell and supercell cases.

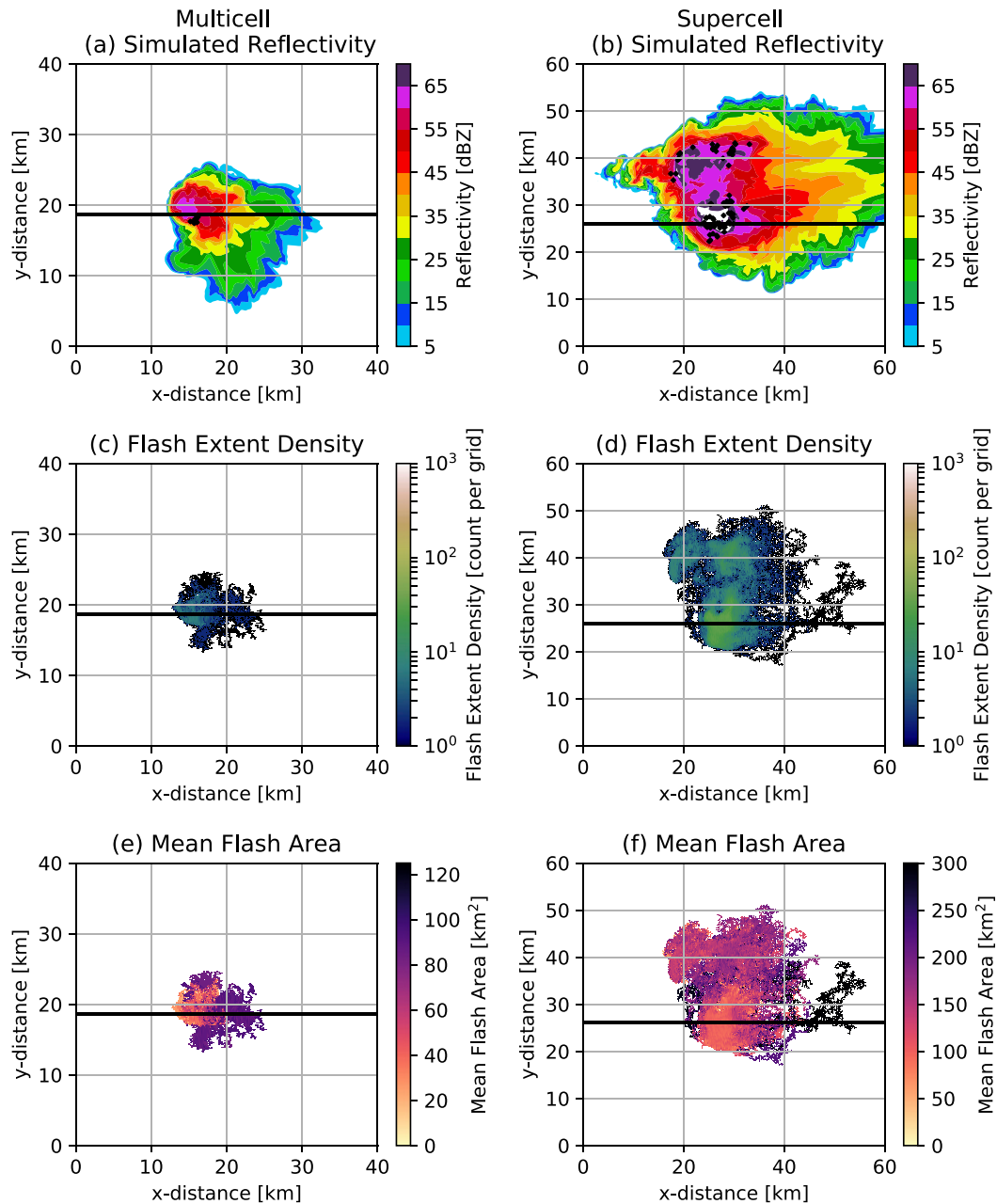


FIG. 3. (a),(b) Simulated composite reflectivity, (c),(d) FED, and (e),(f) mean flash area for both the KTaL071015B and WK supercell cases with 125-m grid spacing. Black diamonds in (a) and (b) represent locations of flash initiations over the previous 30 s. The FED and mean flash area is for each grid cell over the previous 30 s during the storms' peak intensity at 2460 and 3330 s, respectively. The solid black line represents the location of the vertical cross section for Figs. 4–6.

The most striking observation transpired from the net charge structure. The net charge density through the simulated storms, even an ordinary multicellular storm, displayed a much more complex structure, with finer details, than the simple tripole model. These finer details in the net charge density with smaller pockets of charge can be considered as being more textured. Tremendous

amounts of texture were modeled throughout the entire domain of the storm.

This distribution of charge created difficulties in identifying layers of dominant charge at first glance. However, the structure of the electric potential was much simpler and more indicative of a tripolar structure. The reason for the simpler structure was that the electric

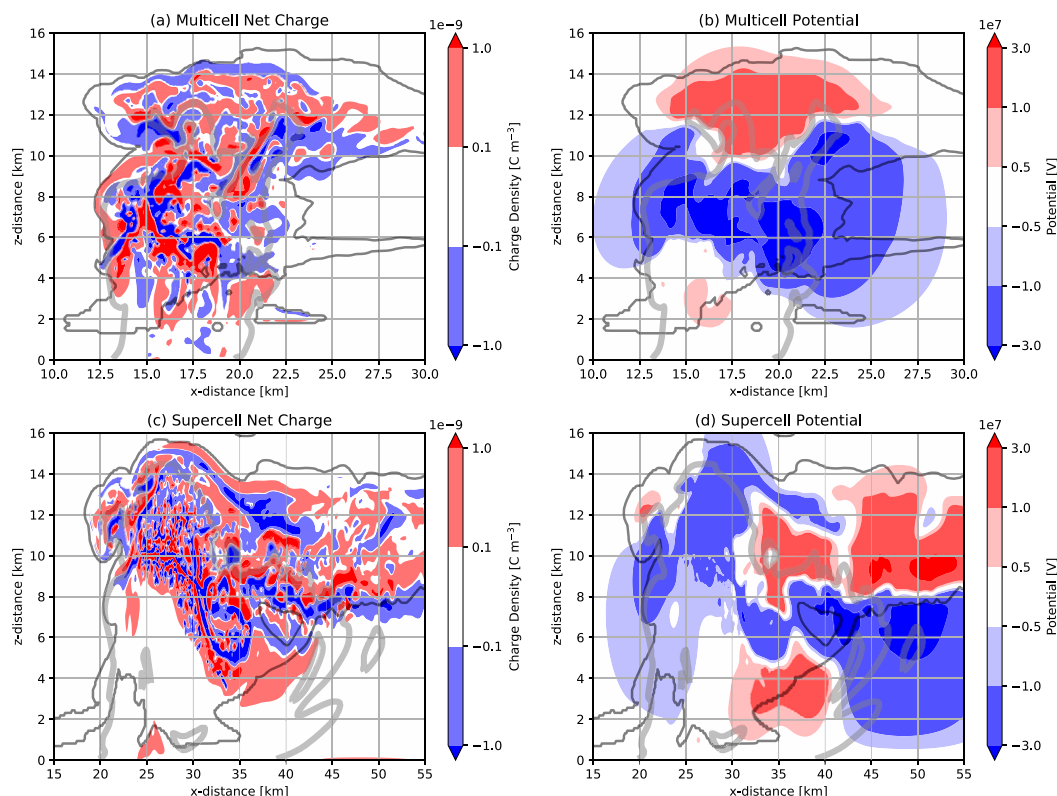


FIG. 4. (left) Vertical cross sections of net charge density (color fill) at intervals of ± 0.1 and 1.0 nC m^{-3} for the (a) KTaL071015B and (c) WK supercell cases. (right) Vertical cross sections of electric potential (color fill) at intervals 5, 10, and 30 MV for the (b) KTaL071015B and (d) WK supercell cases. Additional contours on the cross sections include the 35-dBZ (thick light gray) and cloud boundary (thin dark gray) contours. Location of cross section is highlighted by solid black lines in Fig. 3.

potential acts like an r^{-1} weighted analysis function. Not every region of charge corresponded with a potential well of the same polarity, clarifying that such a simplified mathematical interpretation of electrostatic equations as in Bruning and MacGorman (2013) must emphasize the strong scale dependence. However, the electric potential's sign reflected the sign of the most dominant charge in the local vicinity, and additional charge regions opposite in sign from the dominant charge created perturbations of weaker potential.

a. Spatial distribution of charge budget contributors

When looking at a cross-sectional view of these charge budget contributors within the simulated storms, a perspective can be gained for the spatial contribution of charge for each of these processes. Figure 5 shows the spatial distribution for each term in the charge tendency equation [(1)] for the KTaL071015B simulation along the same vertical cross section as the net charge density in Fig. 4a. The lightning deposition and sedimentation tendencies were the strongest in magnitude and contain opposite signs of charge from each other. The advection

tendencies displayed much finer details of charge tendency than contributors such as the lightning deposition or noninductive charging mechanisms. Throughout the storm, ion drift and diffusional mixing were much smaller than the other four mechanisms though the mixing term was perhaps even more finely textured than charge advection. Similar to Fig. 5, Fig. 6 shows a parallel spatial relationship among all of the charge budget contributors for the WK supercell case. The same general observations from Fig. 5 can be made. The advection tendency appeared to be most like the texture seen in the complex net charge density, while the lightning deposition and sedimentation tendencies showed a large contribution in magnitude but a less variable pattern.

Table 2 presents the magnitude of each of the charge budget contributors for each simulation by summarizing the 99th-percentile gridpoint value for both positive and negative charge tendency and the total positive and negative charge tendency for a single output time. Table 2 additionally provides a general idea for the significance of the magnitude for each charge budget contributor across different simulations. The noninductive

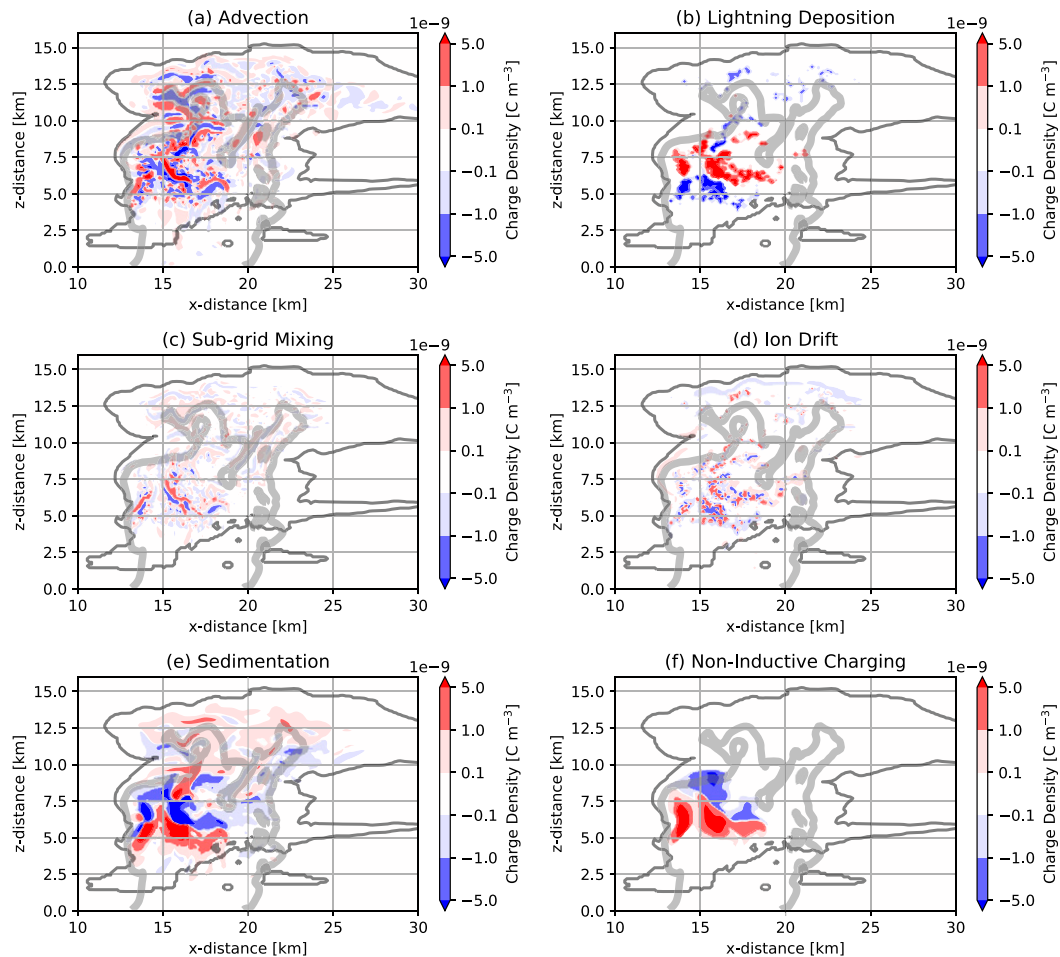


FIG. 5. Vertical cross sections of each net charge contributor (color fill) in the KTaL071015B case at intervals of ± 0.1 , 1.0, and 5.0 nC m^{-3} for the (a) charge advection, (b) lightning deposition, (c) turbulent mixing, (d) ion drift, (e) sedimentation, and (f) noninductive charging mechanisms. Location of cross section is highlighted by solid black line in Fig. 3a.

charging mechanism's 99th percentile showed the largest contribution at any single grid point in both simulations. The sedimentation and lightning deposition tendencies were an order of magnitude less than the noninductive charging mechanism, while the advection, diffusion eddy mixing, and ion drift contributed the least charge at any single grid point. However, when summing up each charge contributor over the entire domain for both simulations, the advection tendency became just as relevant as the sedimentation, lightning deposition, and noninductive charging mechanisms. The diffusional mixing and ion drift's total charge contribution still remained behind the other contributors by at least one order of magnitude.

b. 1D Fourier analysis

1) VERTICAL PROFILES

For each of the simulations in this study, manually chosen locations inside and outside the convective

region of the storm were selected to perform a Fourier analysis of the vertical profile of the charge budget contributors. While all contributors were examined with Fourier analysis, charge advection and lightning deposition illustrated the key differences.

Differences in the advection and lightning deposition tendency discrete spectra are fairly evident in Fig. 7. For the convective region of the multicell case (Fig. 7a), the variance of the advection tendency was spread out over a greater number of, and higher, wavenumbers, while the lightning deposition tendency had a much more concentrated peak at lower wavenumbers. The peak in the advection tendency occurred around 0.75 km^{-1} , while the peak in the lightning deposition tendency occurred around 0.25 km^{-1} . This result suggests that the advection tendency near the updraft region of the storm was most capable of providing a textured contribution to the overall net charge density.

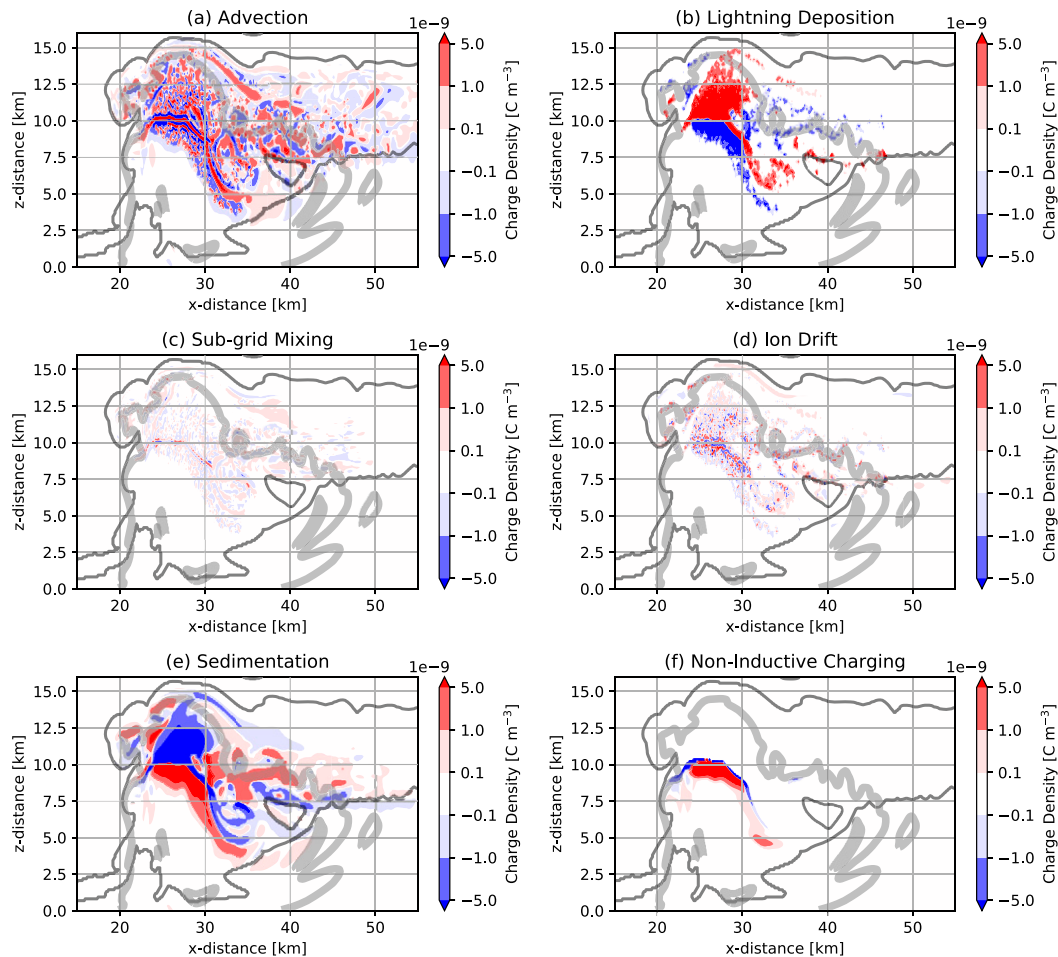


FIG. 6. As in Fig. 5, but for the WK supercell case. Location of cross section is highlighted by solid black line in Fig. 3b.

The Fourier analysis of these charge contributors outside the updraft region (Fig. 7c) shows considerable differences from the convective region of the storm. The variances in both the lightning deposition and advection

tendencies were at least an order of magnitude less outside the updraft region when compared to inside the updraft region. Additionally, the advection tendency's spectra shifted toward lower wavenumbers, suggesting

TABLE 2. The 99th-percentile positive and negative charge tendency at a single grid point and total positive and negative charge tendency summed over the entire domain for the output time at the peak in the simulation's flash rate. Charge tendency values at each grid point are a total accumulation over the previous 30 s. All values are in C m^{-3} .

Simulations	ADV	LGT	SED	MIX	NIC	ION
KTaL071015B						
99th percentile	3.6×10^{-10}	2.9×10^{-9}	2.0×10^{-9}	5.5×10^{-10}	1.5×10^{-8}	1.2×10^{-10}
	-3.9×10^{-10}	-2.2×10^{-9}	-2.8×10^{-9}	-5.0×10^{-10}	-7.5×10^{-9}	-4.0×10^{-11}
Total charge	1.3×10^{-4}	6.6×10^{-5}	1.2×10^{-4}	3.0×10^{-5}	6.3×10^{-5}	4.0×10^{-5}
	-1.3×10^{-4}	-6.6×10^{-5}	-1.2×10^{-4}	-3.0×10^{-5}	-3.9×10^{-5}	-4.0×10^{-5}
WK supercell						
99th percentile	2.4×10^{-9}	1.1×10^{-8}	6.0×10^{-9}	8.6×10^{-10}	6.6×10^{-8}	6.8×10^{-10}
	-2.4×10^{-9}	-9.0×10^{-9}	-9.0×10^{-9}	-8.3×10^{-10}	-4.8×10^{-8}	-5.4×10^{-10}
Total charge	2.1×10^{-3}	2.0×10^{-3}	2.5×10^{-3}	2.4×10^{-4}	1.1×10^{-3}	4.5×10^{-4}
	-2.1×10^{-3}	-2.0×10^{-3}	-2.5×10^{-3}	-2.4×10^{-4}	-9.1×10^{-4}	-4.5×10^{-4}

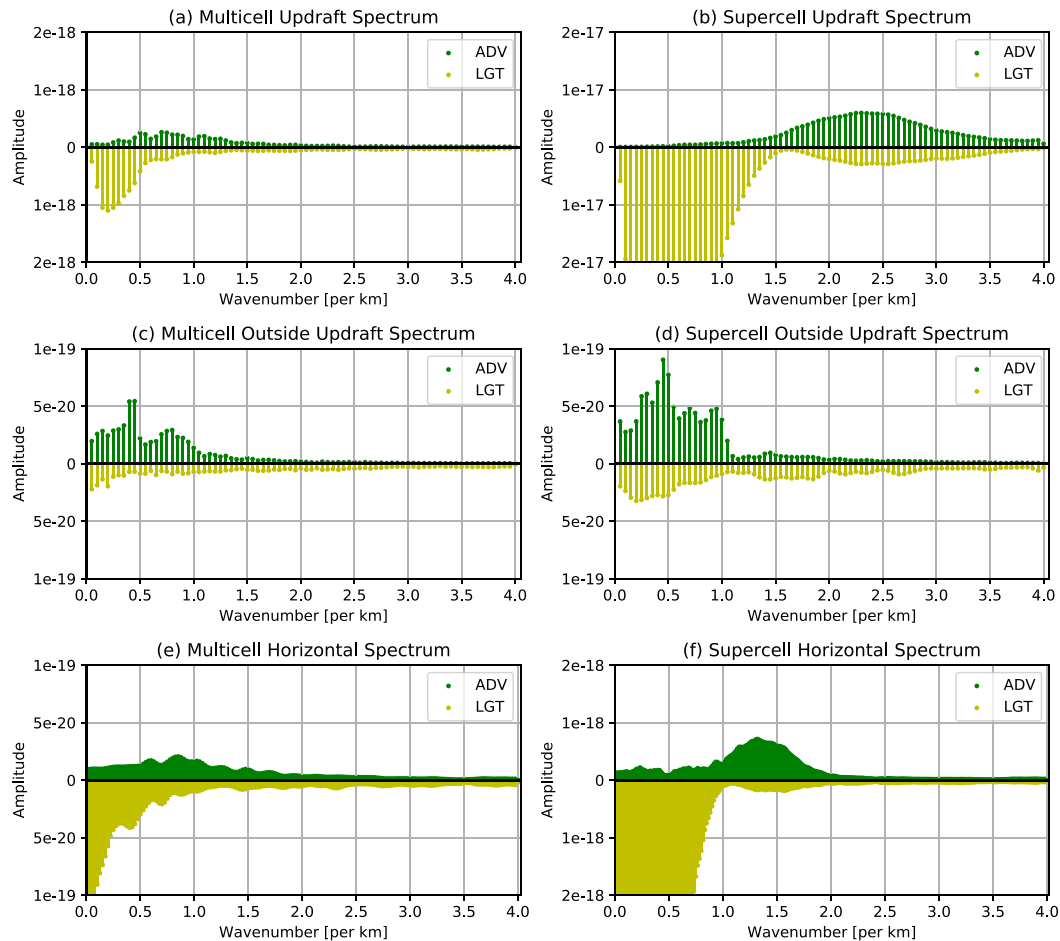


FIG. 7. The discrete spectrum from vertical FFTs for the charge advection (green) and lightning deposition (yellow) tendencies for the convective region of the (a) KTaL071015B and (b) WK supercell simulations and the anvil region of the (c) KTaL071015B and (d) WK supercell simulations. Also included are horizontal FFTs of the (e) KTaL071015B and (f) WK supercell simulations. The lightning deposition spectrum is shown reflected over the x axis. The coordinates selected to represent the convective and anvil regions for each simulation correspond to the following locations in Fig. 3: (15.250, 18.500), (26.875, 25.625), (20.000, 20.500), and (36.250, 26.250) km for (a)–(d), respectively. The location of the horizontal profiles is highlighted by the solid black lines in Fig. 3. The heights of selected horizontal profiles for the KTaL071015B and WK supercell cases were 7.500 and 9.375 km, respectively.

a less textured field as its spectral peak occurred around 0.5 km^{-1} compared to 0.75 km^{-1} near the updraft region. The lightning deposition tendency did not have a distinct spectral peak outside the updraft region of the storm.

The differences in the discrete spectra of advection and lightning deposition tendencies for the supercell case were similar to the multicell simulation; however, these differences were enhanced. For the updraft region of the supercell case (Fig. 7b), once again, the variance of the advection tendency was more spread out over higher wavenumbers, while the lightning deposition tendency had a much more concentrated peak at lower wavenumbers. The magnitude of the variances in the tendency fields were at least an order of magnitude

greater for the WK supercell. Also, the advection tendency spectrum had been shifted to even higher wavenumbers than in the multicell case, with a peak occurring around 2.4 km^{-1} compared to 0.75 km^{-1} , while the peak amplitude increased from roughly 0.25×10^{-18} to $0.70 \times 10^{-17} \text{ C m}^{-3}$. This result would suggest that a higher-flash-rate storm with stronger updraft speeds would have a more textured charge advection tendency.

Additionally, a secondary peak in the lightning deposition tendency occurred around a wavenumber of 2.5 km^{-1} , suggesting that some complexity to the net charge density at high wavenumbers was a result of this charge contributor. Roughly 90% of the variance in the lightning deposition tendency occurred by a wavenumber of 1.25 km^{-1} . The final 10% of the variance took

until a wavenumber of about 3.0 km^{-1} to accumulate, which was due to the secondary peak in the signal's spectrum. This was all while the final 90% of the variance in the advection tendency was being accumulated after a wavenumber of 1.5 km^{-1} . Therefore, the majority of the texture to the net charge density was contributed by advection, while only a small fraction of the lightning charge deposition tendency was providing smaller-scale texture, perhaps as a response to preexisting small-scale texture. A slightly similar occurrence was seen in the KTaL071015B case; however, this was more of an elongated tail than a secondary peak in the lightning charge deposition tendency's spectrum at higher wavenumbers. Still, the presence of the last fraction of variance being accumulated at the highest wavenumbers was shown in the lightning deposition tendency spectrum for both simulations.

Similar to the multicell case, the supercell case displayed comparable differences between the charge contributors inside and outside the convective region of the storm. Figure 7d displays the Fourier analysis outside the updraft region of the supercell case. As was seen in the multicell case, there was a shift in the advection tendency spectrum toward lower wavenumbers, compared to the updraft region, with a spectral peak occurring around 0.5 km^{-1} . Additionally, the variance in the vertical profile of these charge contributors was at least two orders of magnitude less when looking outside the updraft region.

2) HORIZONTAL PROFILES

Since flash area is more related to horizontal scales of charge, Fourier analysis on the horizontal profiles of charge contributors was also conducted. Horizontal profiles across the simulations in the east–west direction (across both convective and anvil regions of storm) were selected at various heights in order to intersect the major charging regions in both storms.

The differences in the advection and lightning deposition discrete spectra distribution were still noticeable. Figures 7e and 7f show the advection tendency spectrum still at higher wavenumbers than the lightning deposition spectrum for both simulations. The advection tendency's peak occurred at 0.75 km^{-1} (same as vertical FFT) for the KTaL071015B case, while the peak of 1.30 km^{-1} in the WK supercell simulation was slightly lower than the vertical Fourier analysis. The lightning deposition tendency spectrum was still concentrated at lower wavenumbers than the advection tendency, and a secondary peak in the WK supercell's lightning deposition spectrum was evident once again. The clear separation between the two charge contributors' spectra was still noticeable regardless the direction in which the

charge contributors are analyzed. That the maxima were not at the same wavenumber indicated the flow within the analysis region was not axisymmetric. Future work could try to identify the orientation of maximum variance and relate it to other properties of the storm cell.

c. Lower-resolution simulations

Each simulation was rerun by only changing the horizontal grid spacing from 125 to 1000 m, while the simulated lightning grid spacing remained at 125-m resolution. This process removed the model's ability to resolve large-eddy motions and was used to test whether or not these motions could be responsible for the complexity seen in the charge structure of the high-resolution simulations.

The electrical activity in the KTaL071015B simulation using 1000-m resolution reached a peak flash rate of 17 min^{-1} with a mean flash area of 30 km^2 . The flash rate and maximum updraft velocity were both smaller by 23% and 25%, respectively, than in the 125-m-resolution simulation. The spatial distribution of flash area population did not drop considerably. The flash areas in Fig. 8e appeared to slightly decrease outside the updraft region compared to the higher-resolution simulation, while the flashes near the updraft region of the storm remained roughly the same area.

Figure 8 also shows the flash extent density (count per grid) and mean flash area (km^2) over the previous 30 s of the WK supercell 1000-m case near the simulation's peak in electrical activity with a flash rate of 75 min^{-1} and mean flash area of 160 km^2 . The flash rate and maximum updraft velocity were both smaller by 57% and 17%, respectively, than in the 125-m-resolution simulation. While not much change in mean flash areas was seen in the KTaL071015B case, the WK supercell case experienced a large jump in mean flash areas compared to the 125-m simulation. This result suggest that a less textured net charge density developed when less complex flow was resolvable, which resulted in overall larger flash areas. The flash areas increased throughout the storm compared to the 125-m simulation. Mean flash areas were nearly 2–3 times larger in the 1000-m simulation near the convective region of the storm and at least 2 times larger in the anvil regions. Figure 9 shows a histogram of flash areas for each simulation at both resolutions highlighting the general increase in flash areas for the WK supercell case.

Figure 10 shows vertical cross sections (along the black lines in Fig. 8) of net charge density and electric potential for both cases using 1000-m grid spacing. The net charge density's distribution appeared less complex, while the electric potential did not show much textural differences from the 125-m-grid-spacing simulations. Even with vertical resolution remaining on a 125-m grid,

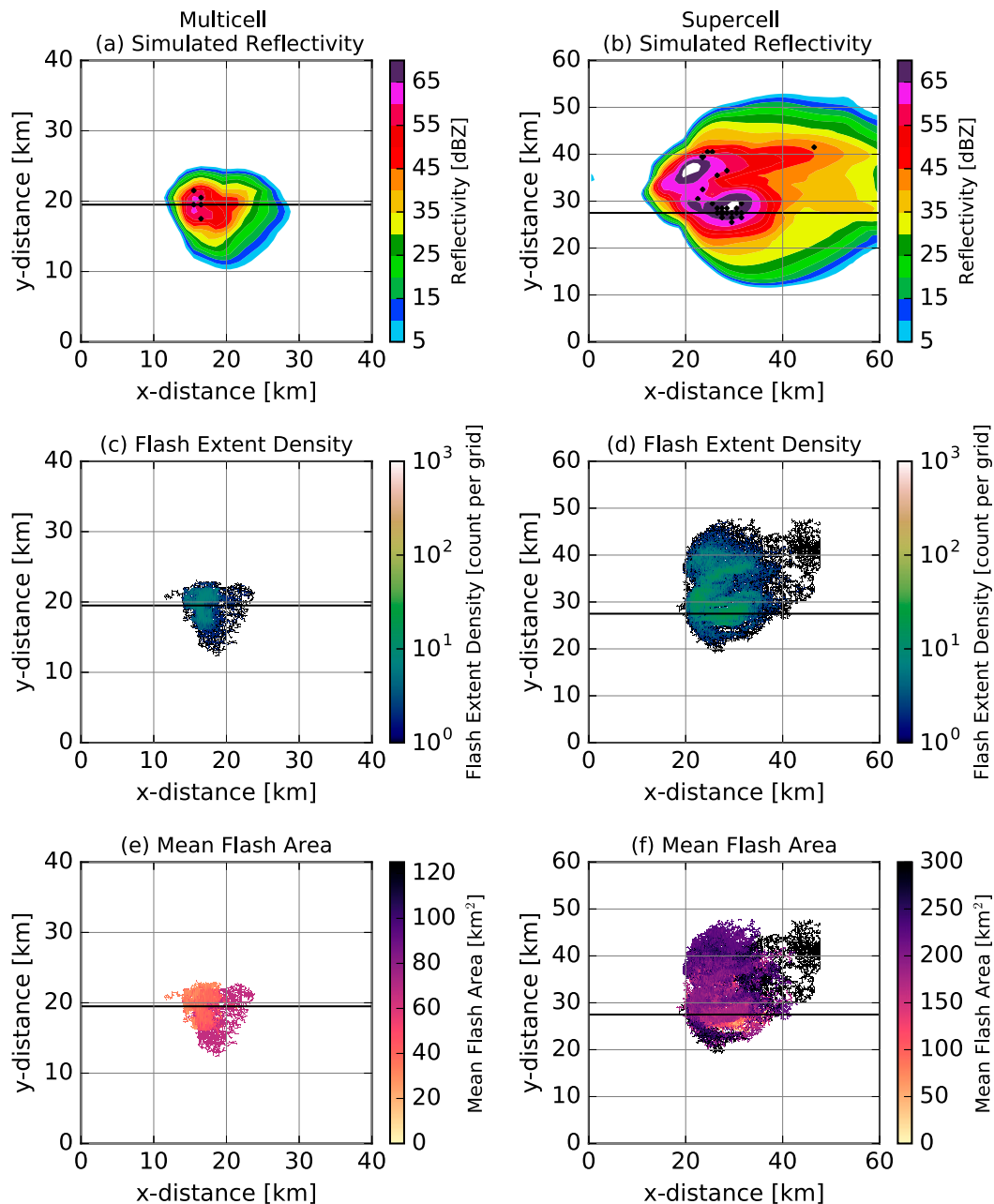


FIG. 8. As in Fig. 3, but for the KTaL071015B and WK supercell cases with 1000-m resolution at 2460 and 3300 s, respectively.

the net charge density did not resemble equivalent texture seen in Fig. 4. To make a more appropriate comparison, Fig. 11 represents the same cross section from Fig. 4, however, with the net charge density and electric potential upscaled to 1000-m horizontal resolution using a top-hat filter. While a simpler charge density pattern existed with the upscaled data, this representation of the charge structure was not equivalent to the textural simplicity seen with the 1000-m-resolution

simulations. The native 1000-m simulations looked artificially layered and choppy, whereas the upscaled versions maintained a wavier, fluidlike structure. This comparison of upscaled high-resolution simulations to coarser-resolution simulations yielded similar results to Bryan et al. (2003) as the better-resolved eddies fundamentally changed the fluid transport.

As a result of the varying-resolution simulations, the potential structure was almost entirely different.

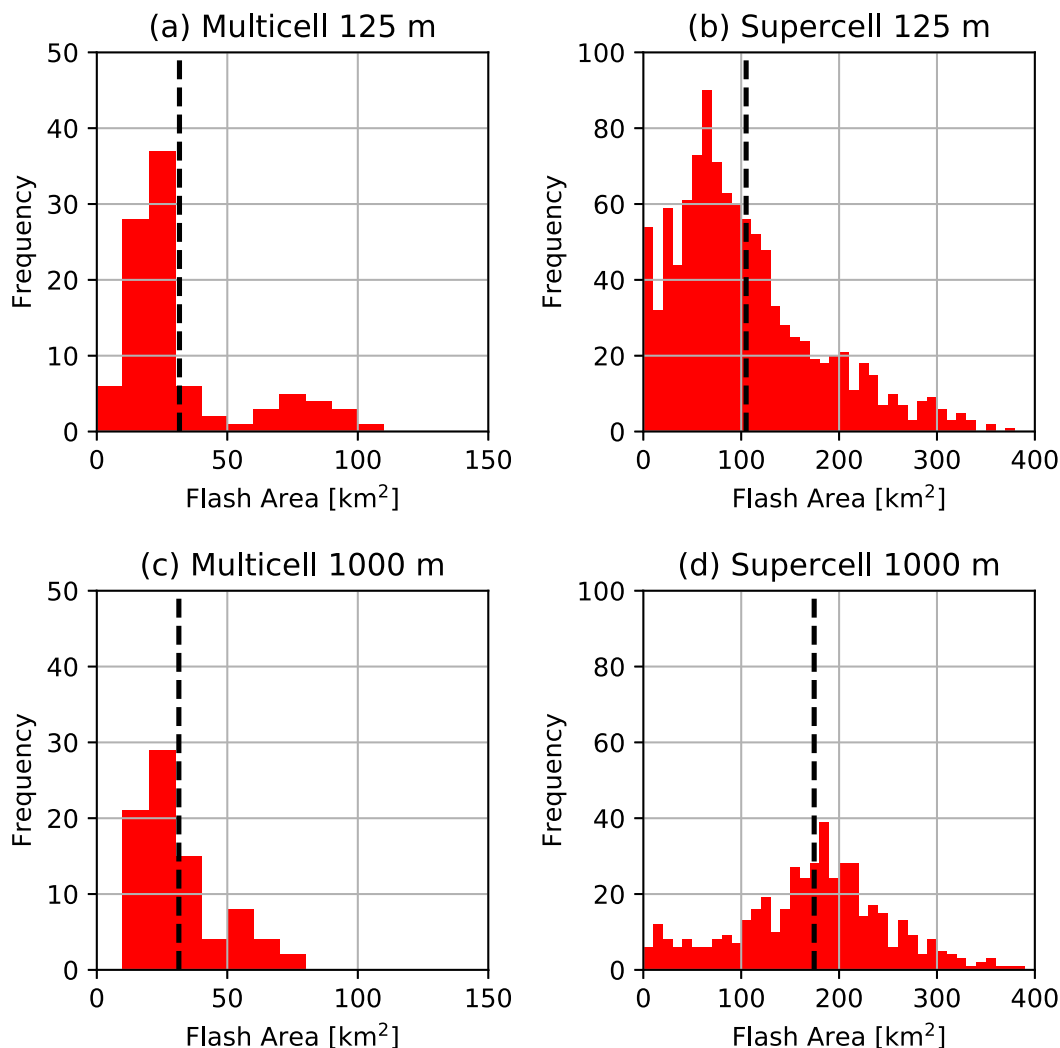


FIG. 9. Histograms of simulated flash area (km^2) for 300 s of each simulation near the peak in electrical activity with both 125- and 1000-m horizontal grid spacing. The vertical dashed black line represents the mean flash area over this 300-s period.

The KTaL071015B case showed similar altitudes of potential maxima; however, the dominant positive charge region moved from 12 to 5 km AGL, and the upper positive charge was substantially weaker with the coarser-resolution simulation. The WK supercell case's potential structure showed more differences in potential locations with different grid spacing, yet the textural complexity remained the same. Additionally, numerous charge contributors experienced changes in structure with the decrease in horizontal resolution. The sedimentation and noninductive charging contributions (not shown) resulted in unbent, regularly shaped, simple structures. Additionally, the subgrid mixing and ion drift contributions (not shown) had smaller spatial coverage compared to the higher-resolution simulations. However, the subgrid mixing term did show values exceeding

1.0 nC m^{-3} in a few concentrated bands, making the magnitude larger in these locations compared to the higher-resolution simulations.

With the largest flash extent densities located near the updraft region of the storm, this variable was chosen as the criterion to systematically check the results from the manually chosen near-updraft locations. Table 3 displays the wavenumber at which 25%, 50%, 75%, and 95% of the accumulated variance occurs from the mean amplitudes of the grid cells among the top 2% of flash extent density values at the peak in the storms' flash rate for both the 125- and 1000-m-resolution simulations. The WK supercell case still showed more texture in the advection tendency than the KTaL071015B simulation, with 25% of the variance accumulating at a wavenumber of 1.69 km^{-1} compared to 0.85 km^{-1} . The KTaL071015B

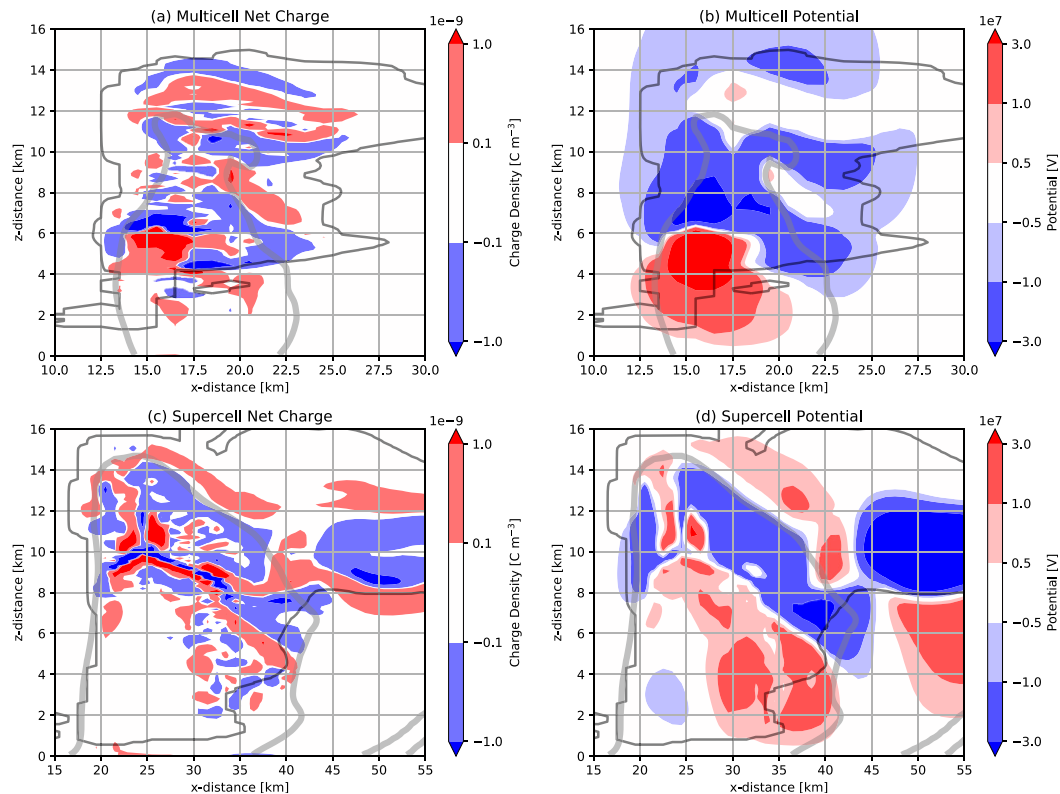


FIG. 10. As in Fig. 4, but for the KTaL071015B and WK supercell cases with 1000-m resolution.

and WK supercell cases experienced a decrease in texture of charge advection tendency with coarser resolution as the wavenumbers at the given thresholds are all less than those for the 125-m-grid-spacing simulations. The same is true for the net charge density as the resolvability of large turbulent eddies was eliminated. This suggests a lack of texture when the model's capability of resolving large eddies is removed. The wavenumbers for the lightning deposition tendency at the given thresholds were fairly similar to each other regardless of the horizontal grid resolution for the WK supercell case. As for the KTaL071015B case, a decrease in lightning deposition texture was observed with the coarser-resolution simulation as the charge density and electric potential took on simpler structures (Table 3 and Fig. 10). Since the simulated branched-lightning grid spacing remained at 125 m for the coarser-resolution simulations, the lightning was responding to smoothed charge and potential fields at 1000-m resolution. Therefore, the resulting lightning deposition tendency was less textured for the multicellular storm simulation at 1000-m resolution. The WK supercell case did not see much change in the lightning deposition texture, but this could be a result of the texture for this simulation's net charge

density, which was more complex than that of the KTaL071015B case.

4. Discussion

The results presented in the previous section reveal the complex and diverse characteristics of the charge budget contributors across two storm modes and sub-storm regions. Synthesis of the data for all simulations was organized by comparing results from inside versus outside the updraft region, advection versus lightning deposition tendency inside the updraft region, high-versus low-flash-rate simulations, and high- versus low-resolution simulations. This provides insight concerning the changes in texture in different regions of the storm, changes in texture for different charge contributors inside the updraft region of the storm, changes in texture with increased electrical activity within a storm, and changes in texture when large-eddy motions are unresolvable.

a. Storm region

Across all of the simulations, the advection tendency had the majority of its spectrum at higher wavenumbers inside the updraft region of the storm in comparison to

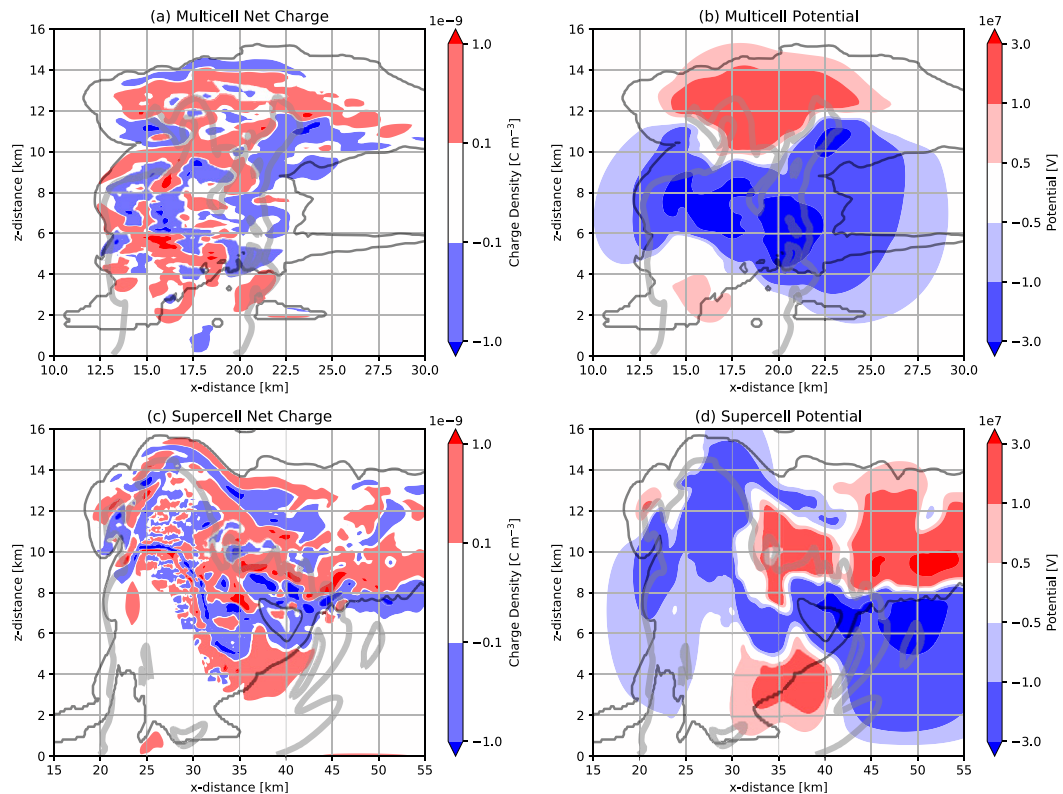


FIG. 11. As in Fig. 4, but for the KTaL071015B and WK supercell cases with 125-m resolution upscaled to 1000-m grid spacing using a top-hat filter.

outside the updraft region. With highly complex flow expected in the updraft region of the storm, this texture in the advection tendency was most likely a result of the overturning of large eddies stirring up charge into smaller pockets. The contribution of smaller pockets of

charge from the advection tendency can be seen near the updraft region of the storm for each simulation in the net charge density. These smaller pockets of net charge, produced with the given resolution, are more conducive to the production of frequent, smaller flashes as a flash

TABLE 3. Wavenumbers (and standard deviation) where 25%, 50%, 75%, and 95% of the total variance accumulates in the charge advection tendency, lightning deposition tendency, and net charge density for the top 2% of FED grid values from each simulation.

	$k > 25\%$	$k > 50\%$	$k > 75\%$	$k > 95\%$
Charge advection tendency				
KTaL071015B 125 m	0.85 ± 0.229	1.32 ± 0.324	1.91 ± 0.450	3.03 ± 0.478
KTaL071015B 1000 m	0.79 ± 0.238	1.12 ± 0.337	1.55 ± 0.400	2.77 ± 0.512
WK supercell 125 m	1.69 ± 0.317	2.18 ± 0.348	2.66 ± 0.385	3.34 ± 0.362
WK supercell 1000 m	1.02 ± 0.304	1.48 ± 0.487	1.98 ± 0.598	2.98 ± 0.505
Lightning deposition tendency				
KTaL071015B 125 m	0.33 ± 0.130	0.52 ± 0.193	1.07 ± 0.414	2.83 ± 0.500
KTaL071015B 1000 m	0.18 ± 0.051	0.27 ± 0.091	0.43 ± 0.137	1.30 ± 0.449
WK supercell 125 m	0.33 ± 0.089	0.57 ± 0.142	0.91 ± 0.217	2.08 ± 0.654
WK supercell 1000 m	0.40 ± 0.188	0.69 ± 0.295	1.22 ± 0.503	2.55 ± 0.821
Net charge density				
KTaL071015B 125 m	0.55 ± 0.222	0.97 ± 0.330	1.46 ± 0.457	2.48 ± 0.539
KTaL071015B 1000 m	0.31 ± 0.101	0.52 ± 0.170	0.78 ± 0.235	1.47 ± 0.356
WK supercell 125 m	0.98 ± 0.377	1.74 ± 0.475	2.54 ± 0.498	3.49 ± 0.335
WK supercell 1000 m	0.47 ± 0.271	0.81 ± 0.334	1.21 ± 0.412	2.12 ± 0.665

will be initiated between regions of potential (typically between regions of charge) where the electric field is greatest and will have more favorable locations for breakdown to occur. This was the case when looking at the mean flash areas for each simulation and how the updraft regions of storms displayed a minimum in mean flash area.

Additionally, outside the updraft region of the storms in each simulation displayed a maximum in mean flash area where the majority of the advection tendency spectrum was at lower wavenumbers. This makes sense with primarily horizontal flow outside the convective region of the storm resulting in less complex charge regions. These less textured charge structures from the advection tendency were most clearly seen in the net charge density downwind from the updraft for each storm. Horizontally layered, less complex charge regions within the storm would be conducive to producing less frequent, larger flashes. It is also important to point out that the spatial distribution of mean flash areas showed consistencies with the storm's charge density and distance from active charging regions. Regions of smaller flash areas were collocated with larger values of charge density and nearby active charge separation regions.

As for the lightning charge deposition tendency, a distinct peak in the spectrum always existed in the updraft region of the storm at a wavenumber between 0 and 1 km^{-1} . However, when considering regions outside the updraft region of the storm, it appeared that there was no common peak among the neighboring vertical profile's spectra being averaged. Additionally, each simulated storm displayed a lightning deposition signal with a variance greater in the updraft region of the storm than outside the updraft region by at least two orders of magnitude. This is most likely due to the lower frequency of flashes occurring outside the updraft region of the storm in all simulations.

b. Comparing charge contributors

When comparing each simulation in the updraft region, variance in the advection tendency spectrum was at higher wavenumbers when compared to the lightning deposition tendency. These higher wavenumbers (smaller wavelengths) in the advection tendency suggest more texture in the signal. With the net charge density being mostly composed of small pockets of charge, the turbulent motions associated with large convective eddies could be providing a considerable amount of charge redistribution through the advection tendency term. The potential exists for even smaller pockets of charge to occur within real thunderstorms; however, the grid resolution limits the scale of turbulent motions being

resolved. On the other hand, the smaller wavenumbers in the lightning deposition tendency suggest a much less textured signal than the advection tendency. The lightning charge deposition appeared to occur in a relatively localized manner, as suggested by Coleman et al. (2003), generally depositing positive charge within the negative potential wells and negative charge within the positive potential wells.

The sedimentation process is another method of distributing charge that was noted before as having a striking resemblance to where, in aggregate, the simulated lightning was occurring. The strongest regions of sedimentation tendency are also generally collocated with noninductive charging maximums. Therefore, complexities in the sedimentation tendency may be masked by the broad swath of charge of a given polarity being placed by these charging regions. Outside the updraft region, complexities can actually be seen in the sedimentation tendency.

c. Varying flash rate

When comparing between storms with varying flash rates, the advection tendency inside the updraft region experienced a spectral power shift to higher wavenumbers in the higher-flash-rate storm. Higher wavenumbers (smaller wavelengths) inside the updraft region of the higher-flash-rate storm suggest an even larger variation in the advection tendency, resulting in a much more textured field. This is consistent with the idea that a much more vigorous updraft would be wider and support more separate regions of charge in a more complex thunderstorm flow structure. Additionally, the differences in storm size for the KTaL071015B ($15 \text{ km} \times 15 \text{ km}$) and WK supercell ($35 \text{ km} \times 35 \text{ km}$) cases result in a smaller ratio between the model resolution and the feature being simulated for the multicell case. Therefore, fewer large eddies may be resolved with the smaller storm size creating a less textured charge advection tendency.

As for the lightning deposition tendency, a fairly similar spectrum was seen across all simulations with varying storm modes inside the updraft region of the storm. The higher-flash-rate storms did exhibit slightly more texture than the lower-flash-rate cases did; however, this is only indicated by a slight shift in the spectral peaks from 0.25 to 0.5 km^{-1} . This suggests that, regardless of the storm mode, lightning deposition will always contribute to a less textured field. However, the WK supercell case displayed a feature in its lightning deposition spectrum that was not clearly identifiable in any of the other simulations. The smaller secondary peak in its spectrum at higher wavenumbers (2.5 km^{-1}) could be the product of smaller flashes occurring in

smaller regions of charge within the storm and therefore complicating the net charge structure on the smaller scale. However, it is still not clear whether these lightning channels were the initial force for creating a complicated net charge structure within the simulations. The secondary peak in the lightning deposition tendency spectrum was an occurrence not identified in the KTaL071015B case potentially because of less turbulent energy being unable to stir up charge into these smaller pockets. Since the spectral position of the charge advection and secondary peak in the lightning deposition matched, sufficient potential can still reside at smaller scales with storms containing faster (more turbulent) updrafts.

Spectra outside the updraft region, for both advection and lightning deposition tendencies, remained fairly consistent across all storm modes. This coincides with the notion that regions farther away from the storm's updraft contained less complex, primarily horizontal flow regardless of storm mode, resulting in less textured, more stratified charge regions when compared to the updraft region. Additionally, fewer lightning flashes will occur outside the updraft region of the storm compared to near the updraft, and therefore, the lightning deposition will provide the same amount of texture no matter what storm mode is present.

d. Varying horizontal resolution

When comparing the charge contributors of the simulated storms using 125- and 1000-m horizontal resolution, the charge advection tendency still displayed the most texture using both resolutions; however, this process contributed less overall charge in the 1000-m simulations. The KTaL071015B and WK supercell cases exhibited a decrease in texture of charge advection tendency as coarser resolution eliminated the resolvability of large turbulent eddies. This agrees with the concept that the resolved flow (since large-eddy and inertial-range turbulent flow is not resolved at 1000-m grid spacing) cannot develop narrow regions of charge and therefore cannot produce as small of flash areas. The texture comparison between these simulations at different resolutions was only evaluated along the vertical axis, which did not change in resolution with the 1000-m simulations (only horizontal resolution changed).

Bruning and MacGorman (2013) discussed how the kinematic and electrical characteristics of a storm are coupled. If a storm shows an updraft burst or even has a faster updraft than another storm, more turbulent flow will be associated with that motion and therefore generate smaller flash areas as a result. By removing more of the smaller-scale unsteady flow within these simulations, the reduction of small flashes supports the notion that these two thunderstorm properties are associated with each other.

e. Limitations and future work

As with any modeling study, numerous uncertainties and limitations arise from the assumptions made, including choices about cloud ice microphysics and how they influence the charging parameterization. Uncertainties of particular importance to this study are those that introduce scale-dependent spatial structure. The stochastic branched-lightning scheme of Mansell (2002), which affects how the lightning propagates and deposits charge, vastly simplifies the lightning process, which in reality has strongly varying current and channel conductivity. The parameterization assumes that good conductivity is maintained across all branches and between the positive and negative ends. This could affect how lightning responds to variations in the potential. Additionally, simulated channels span the width of the grid rather than a few centimeters, which may also reduce the response to small-scale features. As for the model resolution, 125-m grid spacing should be sufficient enough to simulate deep moist convection with large-eddy motions, as suggested by Bryan et al. (2003), yet this still might not be enough resolution to reproduce the true electrical nature of observed storms. These could all be reasons as to why the modeled flash sizes are larger than those from observational studies with LMA data such as Schultz et al. (2015) and Zhang et al. (2017).

Further work can be done to evaluate advection tendency's role of complicating charge structures in order to distinguish where the advection tendency is creating new texture or moving around existing texture. Shear zones normal to charge gradients could be a source of increased texture; however, this component cannot be separated from advection of existing texture without a Lagrangian approach. Examining the behavior of a group of trajectories tracking positive charge to see if they diverge from each other or follow them backward to see if separate regions had been previously contiguous could provide valuable insight into the specifics of charge advection's role.

Aside from the advection and lightning deposition tendencies, the potential remains for the fluctuating updraft to also create rapid changes to other charge-contributing fields such as the sedimentation or non-inductive charging tendencies. Rapid updraft evolution could relocate or develop new charging regions or alter how hydrometeor fallout occurs, which could also produce complexities to the net charge density. However, in aggregate effect, this behavior was not observed. Also, the Fourier analysis conducted in this study looks at charge tendencies accumulated over the previous 30 s. The possibility exists for various charge contributors to provide varying amounts of texture on different time

scales. This study looked at the texture seen in these charge-contributing fields near the peak in the simulations' electrical activity where complex charge structures already existed. Future studies could investigate which forcing is most responsible for the initial development of complex charge structures. Therefore, the advection tendency might not be the only charge contributor most capable of affecting flash behavior near the updraft region of the storm despite not knowing whether or not this process introduced texture initially.

Responses to supercell or multicell updraft surges have been seen in LMA data with increases in smaller flash areas and vertical rise of source points near the updraft region of the storm (Bruning et al. 2010; Calhoun et al. 2013). These surges may create new charge separation centers or penetrate previous regions. This leads to the potential to explore flash area spectra, like those presented in Bruning and MacGorman (2013), to look for whether a separate peak for smaller flashes is also observed within storms during updraft surges. If these surges are identified within the model simulations, texture comparisons of the net charge density and charge contributors can be made before and after these updraft surges. This could provide further evidence for the coupling of kinematic and electrical characteristics of a storm and insights to which process is most responsible for complicating the charge structure initially.

With the propagation of a lightning channel remaining within a potential well (MacGorman et al. 2001; Coleman et al. 2003; Mansell et al. 2010), each flash should as well generally remain within regions of charge for mathematical reasons described by Bruning and MacGorman (2013). However, modeling results showed that not every region of charge, typically those smaller in size, was reflected by a potential well of that same sign but rather a perturbation to the overall electric potential that reflected the most dominant charge regions. The electric potential from these simulations is what most similarly appeared to represent a tripolar structure, not the net charge density. Therefore, it might be better to consider impacts the charge tendencies had on the electric potential, which lightning channel propagation would respond more directly to, and not treat the two quantities as equivalents. Since in aggregate, the lightning channels primarily react to the electric potential, future studies might investigate which of these charge tendencies contributes most to the overall potential field. Each of these charge contributors could be run through a Poisson solver in order to retrieve the components of the "potential budget." Fourier analysis could be conducted to identify the texture of these potential budget contributors, as this method would more

directly show the impacts of charge separation and redistribution on the lightning flash areas.

While in aggregate, the lightning deposition responded to the smoother potential field, there was some evidence that individual flashes responded to the fine texture in the net charge and advection fields. The WK supercell simulations in particular show this with a secondary peak in lightning deposition matched to the scale of charge advection. Furthermore, in all cases the horizontal extent of flashes was smaller on average in regions of the storm with more charge texture. While it needs more study in light of the limitations just noted, these results suggest that individual flashes respond to small-scale perturbations to potential caused by charge, while in aggregate, charge is deposited in a smoother manner consistent with reduction of net electric potential energy in the storm. An analysis of the Fourier decomposition of all contributors confirms this analysis. Lightning deposition at lower wavenumbers is of similar magnitude to sedimentation and noninductive charging, while the lightning deposition at higher wavenumbers is closer to the charge advection, with sedimentation and noninductive charging rapidly decreasing in magnitude at smaller scales.

5. Conclusions

This study assessed the charge budget contributors within a simulated thunderstorm using the Collaborative Model for Multiscale Atmospheric Simulation. Storms were modeled using an atmospheric sounding from the Kinematic Texture and Lightning field campaign at Texas Tech University along with the classic Weisman and Klemp sounding to provide a variety of storm-mode cases for this study. The net charge structure observed in these simulations displayed much more complexity than is typically visualized in the literature; these simplistic illustrations may in fact better summarize potential in many storms. The lightning deposition, sedimentation, and noninductive charging tendencies were the largest contributors to the charge budget but were limited to only a few larger pockets of charge within the storms. The lightning deposition tendency generally matched the spatial distribution of the sedimentation tendency, and both corresponded well with the electric potential. The charge advection tendency transported similar amounts of charge, but it was spread out into smaller neighboring pockets throughout various regions of the storm, providing a source of texture to the net charge density but not significantly altering the overall potential structure. The ion drift and diffusional mixing tendencies contributed much less overall charge than the other four mechanisms.

Comparisons of texture between the lightning deposition and charge advection tendencies revealed more textured charge advection profiles (in amplitude at higher wavenumbers), especially for higher-flash-rate storms with larger maximum updraft speeds. The lightning deposition tendency's texture remained fairly consistent among varying storm modes with high-flash-rate storms contributing some small-scale texture to the net charge density. The charge advection tendency was more textured inside the updraft region of the storms where more resolved eddy-rich flow was present. The texture of the charge advection tendency and net charge density decreased in the KTaL071015B and WK supercell cases when removing the model's ability to resolve large-eddy motions in the 1000-m-resolution simulations.

All of these charge budget contributors provided varying contribution to the overall net charge density. The clear scale separation between the advection and lightning deposition tendencies suggests that charge advection is the larger contributor of net charge texture where complex flow is present. This study also provides further evidence of the coupling between the kinematic and electrical characteristics of a storm, as suggested by Bruning and MacGorman (2013), but does not provide a clear-cut answer to the question of which process produces net charge texture in the first place. Future work should account for the scale-dependent differences in charge and potential, with attention paid to differences in the instantaneous response of individual flashes versus aggregate behavior. These potential contributors can also be investigated further in relation to updraft surges seen within storms in an attempt to further derive the cause of net charge complexity.

Acknowledgments. Much of this work composed the master's degree thesis of Mr. Brothers at Texas Tech University. We thank Vicente Salinas and Dr. Johannes Dahl of Texas Tech University's Department of Geosciences' Atmospheric Science Group for their helpful contributions providing comments, ideas, and interest over the course of this study. Additionally, we thank Texas Tech University's High Performance Computing Center (HPCC) for providing the resources to conduct the model simulations presented in this study. This study was supported by the National Science Foundation Award AGS-1352144 under the CAREER Program.

REFERENCES

- Bruning, E. C., and D. R. MacGorman, 2013: Theory and observations of controls on lightning flash size spectra. *J. Atmos. Sci.*, **70**, 4012–4029, <https://doi.org/10.1175/JAS-D-12-0289.1>.
- , W. D. Rust, D. R. MacGorman, M. I. Biggerstaff, and T. J. Schuur, 2010: Formation of charge structures in a supercell. *Mon. Wea. Rev.*, **138**, 3740–3761, <https://doi.org/10.1175/2010MWR3160.1>.
- Bryan, G. H., J. C. Wyngaard, and J. M. Fritsch, 2003: Resolution requirements for the simulation of deep moist convection. *Mon. Wea. Rev.*, **131**, 2394–2416, [https://doi.org/10.1175/1520-0493\(2003\)131<2394:RRFTSO>2.0.CO;2](https://doi.org/10.1175/1520-0493(2003)131<2394:RRFTSO>2.0.CO;2).
- Calhoun, K. M., D. R. MacGorman, C. L. Ziegler, and M. I. Biggerstaff, 2013: Evolution of lightning activity and storm charge relative to dual-Doppler analysis of a high-precipitation supercell storm. *Mon. Wea. Rev.*, **141**, 2199–2223, <https://doi.org/10.1175/MWR-D-12-00258.1>.
- , E. R. Mansell, D. R. MacGorman, and D. C. Dowell, 2014: Numerical simulations of lightning and storm charge of the 29–30 May 2004 Geary, Oklahoma, supercell thunderstorm using EnKF mobile radar data assimilation. *Mon. Wea. Rev.*, **142**, 3977–3997, <https://doi.org/10.1175/MWR-D-13-00403.1>.
- Chmielewski, V. C., and E. C. Bruning, 2016: Lightning Mapping Array flash detection performance with variable receiver thresholds. *J. Geophys. Res. Atmos.*, **121**, 8600–8614, <https://doi.org/10.1002/2016JD025159>.
- Coleman, L. M., T. C. Marshall, M. Stolzenburg, T. Hamlin, P. R. Krehbiel, W. Rison, and R. J. Thomas, 2003: Effects of charge and electrostatic potential on lightning propagation. *J. Geophys. Res.*, **108**, 4298, <https://doi.org/10.1029/2002JD002718>.
- Fierro, A. O., and E. R. Mansell, 2017: Electrification and lightning in idealized simulations of a hurricane-like vortex subject to wind shear and sea surface temperature cooling. *J. Atmos. Sci.*, **74**, 2023–2041, <https://doi.org/10.1175/JAS-D-16-0270.1>.
- Gunter, W. S., and J. L. Schroeder, 2015: High-resolution full-scale measurements of thunderstorm outflow winds. *J. Wind Eng. Ind. Aerodyn.*, **138**, 13–26, <https://doi.org/10.1016/j.jweia.2014.12.005>.
- Halbert, K. T., G. W. Blumberg, and P. T. March, 2015: SHARPy: Fueling the Python cult. *95th Amer. Meteor. Soc. Annual Meeting*, Phoenix, AZ, Amer. Meteor. Soc., 1.402, <https://ams.confex.com/ams/95Annual/webprogram/Paper270233.html>.
- Hay, G., K. Niemann, and G. McLean, 1996: An object-specific image-texture analysis of H-resolution forest imagery. *Remote Sens. Environ.*, **55**, 108–122, [https://doi.org/10.1016/0034-4257\(95\)00189-1](https://doi.org/10.1016/0034-4257(95)00189-1).
- Herold, M., X. Liu, and K. C. Clarke, 2003: Spatial metrics and image texture for mapping urban land use. *Photogramm. Eng. Remote Sensing*, **69**, 991–1001, <https://doi.org/10.14358/PERS.69.9.991>.
- Klemp, J. B., and R. B. Wilhelmson, 1978: Simulations of right- and left-moving storms produced through storm splitting. *J. Atmos. Sci.*, **35**, 1097–1110, [https://doi.org/10.1175/1520-0469\(1978\)035<1097:SORALM>2.0.CO;2](https://doi.org/10.1175/1520-0469(1978)035<1097:SORALM>2.0.CO;2).
- Logan, T. L., A. H. Strahler, and C. E. Woodcock, 1979: Use of a standard deviation based texture channel for Landsat classification of forest strata. *Machine Processing of Remotely Sensed Data Symp.*, West Lafayette, IN, Institute of Electrical and Electronics Engineers, 395.
- MacGorman, D. R., J. M. Straka, and C. L. Ziegler, 2001: A lightning parameterization for numerical cloud models. *J. Appl. Meteor.*, **40**, 459–478, [https://doi.org/10.1175/1520-0450\(2001\)040<0459:ALPFNC>2.0.CO;2](https://doi.org/10.1175/1520-0450(2001)040<0459:ALPFNC>2.0.CO;2).
- Mansell, E. R., 2002: Simulated three-dimensional branched lightning in a numerical thunderstorm model. *J. Geophys. Res.*, **107**, 4075, <https://doi.org/10.1029/2000JD000244>.
- , and C. L. Ziegler, 2013: Aerosol effects on simulated storm electrification and precipitation in a two-moment bulk

- microphysics model. *J. Atmos. Sci.*, **70**, 2032–2050, <https://doi.org/10.1175/JAS-D-12-0264.1>.
- , D. R. MacGorman, C. L. Ziegler, and J. M. Straka, 2005: Charge structure and lightning sensitivity in a simulated multicell thunderstorm. *J. Geophys. Res.*, **110**, D12101, <https://doi.org/10.1029/2004JD005287>.
- , C. L. Ziegler, and E. C. Bruning, 2010: Simulated electrification of a small thunderstorm with two-moment bulk microphysics. *J. Atmos. Sci.*, **67**, 171–194, <https://doi.org/10.1175/2009JAS2965.1>.
- Mazur, V., 2002: Physical processes during development of lightning flashes. *C. R. Phys.*, **3**, 1393–1409, [https://doi.org/10.1016/S1631-0705\(02\)01412-3](https://doi.org/10.1016/S1631-0705(02)01412-3).
- Reynolds, S. E., M. Brook, and M. F. Gourley, 1957: Thunderstorm charge separation. *J. Meteor.*, **14**, 426–436, [https://doi.org/10.1175/1520-0469\(1957\)014<0426:TCS>2.0.CO;2](https://doi.org/10.1175/1520-0469(1957)014<0426:TCS>2.0.CO;2).
- Rison, W., R. J. Thomas, P. R. Krehbiel, T. Hamlin, and J. Harlin, 1999: A GPS-based three-dimensional lightning mapping system: Initial observations in central New Mexico. *Geophys. Res. Lett.*, **26**, 3573–3576, <https://doi.org/10.1029/1999GL010856>.
- Saunders, C., 2008: Charge separation mechanisms in clouds. *Space Sci. Rev.*, **137**, 335–353, <https://doi.org/10.1007/s11214-008-9345-0>.
- , and S. L. Peck, 1998: Laboratory studies of the influence of the rime accretion rate on charge transfer during crystal/graupel collisions. *J. Geophys. Res.*, **103**, 13 949–13 956, <https://doi.org/10.1029/97JD02644>.
- Schultz, C. J., L. D. Carey, E. V. Schultz, and R. J. Blakeslee, 2015: Insight into the kinematic and microphysical processes that control lightning jumps. *Wea. Forecasting*, **30**, 1591–1621, <https://doi.org/10.1175/WAF-D-14-00147.1>.
- Shao, X. M., and P. R. Krehbiel, 1996: The spatial and temporal development of intracloud lightning. *J. Geophys. Res.*, **101**, 26 641–26 668, <https://doi.org/10.1029/96JD01803>.
- Stolzenburg, M., W. D. Rust, and T. C. Marshall, 1998: Electrical structure in thunderstorm convective regions: 2. Isolated storms. *J. Geophys. Res.*, **103**, 14 079–14 096, <https://doi.org/10.1029/97JD03547>.
- Takahashi, T., 1978: Riming electrification as a charge generation mechanism in thunderstorms. *J. Atmos. Sci.*, **35**, 1536–1548, [https://doi.org/10.1175/1520-0469\(1978\)035<1536:REAACG>2.0.CO;2](https://doi.org/10.1175/1520-0469(1978)035<1536:REAACG>2.0.CO;2).
- Weisman, M. L., and J. B. Klemp, 1982: The dependence of numerically simulated convective storms on vertical wind shear and buoyancy. *Mon. Wea. Rev.*, **110**, 504–520, [https://doi.org/10.1175/1520-0493\(1982\)110<0504:TDonSC>2.0.CO;2](https://doi.org/10.1175/1520-0493(1982)110<0504:TDonSC>2.0.CO;2).
- Wicker, L. J., and R. B. Wilhelmson, 1995: Simulation and analysis of tornado development and decay within a three-dimensional supercell thunderstorm. *J. Atmos. Sci.*, **52**, 2675–2703, [https://doi.org/10.1175/1520-0469\(1995\)052<2675:SAAOTD>2.0.CO;2](https://doi.org/10.1175/1520-0469(1995)052<2675:SAAOTD>2.0.CO;2).
- Williams, E. R., M. E. Weber, and R. E. Orville, 1989: The relationship between lightning type and convective state of thunderclouds. *J. Geophys. Res.*, **94**, 13 213–13 220, <https://doi.org/10.1029/JD094iD11p13213>.
- Zhang, Z., D. Zheng, Y. Zhang, and G. Lu, 2017: Spatial-temporal characteristics of lightning flash size in a supercell storm. *Atmos. Res.*, **197**, 201–210, <https://doi.org/10.1016/j.atmosres.2017.06.029>.
- Ziegler, C. L., 1985: Retrieval of thermal and microphysical variables in observed convective storms. Part 1: Model development and preliminary testing. *J. Atmos. Sci.*, **42**, 1487–1509, [https://doi.org/10.1175/1520-0469\(1985\)042<1487:ROTAMV>2.0.CO;2](https://doi.org/10.1175/1520-0469(1985)042<1487:ROTAMV>2.0.CO;2).